Three-step nucleation of metal–organic framework nanocrystals

Xiangwen Liu[a,b], See Wee Chee[a,b,c], Sanoj Raj[d], Michal Sawczyk[d], Petr Král[d,e,f], and Utkur Mirsaidov[a,b,c,g,1]

[a]Department of Physics, National University of Singapore, Singapore 117551, Singapore; [b]Centre for BioImaging Sciences, Department of Biological Sciences, National University of Singapore, Singapore 117557, Singapore; [c]Centre for Advanced 2D Materials and Graphene Research Centre, National University of Singapore, Singapore 117546, Singapore; [d]Department of Chemistry, University of Illinois at Chicago, Chicago, IL 60607; [e]Department of Physics, University of Illinois at Chicago, Chicago, IL 60607; [f]Department of Pharmaceutical Sciences, University of Illinois at Chicago, Chicago, IL 60607; and [g]Department of Materials Science and Engineering, National University of Singapore, Singapore 117575, Singapore

Edited by Omar M. Yaghi, University of California, Berkeley, CA, and approved January 8, 2021 (received for review May 13, 2020)

Metal–organic frameworks (MOFs) are crystalline nanoporous materials with great potential for a wide range of industrial applications. Understanding the nucleation and early growth stages of these materials from a solution is critical for their design and synthesis. Despite their importance, the pathways through which MOFs nucleate are largely unknown. Using a combination of in situ liquid-phase and cryogenic transmission electron microscopy, we show that zeolitic imidazolate framework-8 MOF nanocrystals nucleate from precursor solution via three distinct steps: 1) liquid–liquid phase separation into solute-rich and solute-poor regions, followed by 2) direct condensation of the solute-rich region into an amorphous aggregate and 3) crystallization of the aggregate into a MOF. The three-step pathway for MOF nucleation shown here cannot be accounted for by conventional nucleation models and provides direct evidence for the nonclassical nucleation pathways in open-framework materials, suggesting that a solute-rich phase is a common precursor for crystallization from a solution.

crystallization | nucleation | in situ TEM | MOF

Metal–organic frameworks (MOFs) with highly porous crystalline structures are an important class of multifunctional materials for applications in catalysis (1), gas storage (2), and separation (3) because of their tunable pore structures (4). Generally, these MOF crystals form from a solution containing metal ions and organic linkers, where the linkers react with the ions to connect them into the final porous structure (5). The crystallization of MOFs and the states leading up to the crystallization influence their nucleation rates (6), porous network structure, and polymorphism (7). Hence, detailed insight into the nucleation of MOFs is critical for their synthesis and tailoring their properties for specific applications. However, the details of the nucleation and early growth stages of MOFs are unknown because they are extremely challenging to probe (8, 9).

Broadly speaking, the accurate description of a nucleation process in a solution is a challenge that is common to biology, chemistry, geology, and materials science (10). The conventional description of the nucleation is based on the classical nucleation theory (CNT), which assumes that crystals grow directly from stable crystalline nuclei that form in a solution in a spontaneous manner (11–14). However, in many cases, CNT cannot adequately describe the nucleation processes (10, 15); the nucleation rates from the experiments are often many orders of magnitudes faster than those predicted from the CNT. In order to account for this and other differences, alternative, nonclassical nucleation models with an additional step(s) preceding the crystallization have been proposed (11, 16–20). These models are often used to describe the nucleation of metals (21, 22), lysozymes (12, 23), and carbonates (24–26). For example, in the latter case, amorphous calcium carbonate (ACC) serves as a precursor for crystalline $CaCO_3$, and ACC itself either forms in a solution through the aggregation of small prenucleation clusters or emerges from a dense liquid phase rich in solutes or grows from an amorphous nucleus (27). Even for this extensively studied system, the abundance of possible crystallization pathways makes identifying the parameters that govern the intermediate prenucleation steps extremely challenging.

In the case of MOFs, despite their importance in many applications, the detailed stages of crystallization are even less clear (8). Among several competing models that have been proposed to explain their nucleation and growth, two are the most prevalent. The first one follows the classical pathway, which stipulates that MOF crystals grow by the addition of monomers to spontaneously formed stable crystalline nuclei (28, 29). The second pathway proposes that MOFs nucleate through a nonclassical route comprising multiple steps. Here, monomers in solution first form small clusters containing metal ions and linkers, and then these clusters aggregate into amorphous nanoparticles, followed by the crystallization that starts deep within these nanoparticles (28, 30–32). The difficulty in capturing the different stages of the MOF nucleation, which is necessary for resolving the debate around the different nucleation mechanisms, stems from the lack of suitable experimental approaches that can directly track the evolution of individual crystals (8). While in situ TEM had been used to study the postnucleation growth of MOFs, these nucleation pathways still remain elusive due to the experimental challenges associated with the electron-beam-sensitive nature of MOFs (33). Here, using direct time-resolved in situ transmission electron microscopy (TEM) imaging at very low electron fluxes, we show that MOFs form by a liquid–liquid phase separation of the reaction solution into solute-rich and solute-poor

Significance

Nucleation is ubiquitous in many natural and industrial processes, yet our understanding of how a nucleus first emerges is limited. According to classical nucleation theory, a nucleus from which crystals grow forms in a single, spontaneous step. In this work, we combine ultralow-dose in situ liquid-phase and cryogenic transmission electron microscopy to show that metal–organic frameworks (MOFs) nucleate through a different, nonclassical pathway with three distinct steps. These steps are phase separation, condensation, and crystallization. Our observations of intermediate steps during the crystallization of MOFs provide important insight for controlling the nucleation and growth of both crystalline and amorphous materials.

Author contributions: X.L. and U.M. designed research; X.L. performed research; S.R., M.S., and P.K. performed molecular dynamics simulations; X.L., S.W.C., and U.M. analyzed data; and X.L., P.K., and U.M. wrote the paper.

The authors declare no competing interest.

This article is a PNAS Direct Submission.

[1]To whom correspondence may be addressed. Email: mirsaidov@nus.edu.sg.

This article contains supporting information online at https://www.pnas.org/lookup/suppl/doi:10.1073/pnas.2008880118/-/DCSupplemental.

Published March 1, 2021.

regions, followed by condensation of the solute-rich phases into dense aggregates, which then crystallize into MOF nanocrystals.

Results and Discussion

Capturing the nucleation of MOFs with TEM is challenging because these crystals are extremely beam sensitive and damage easily during imaging (34). Here, we extend the in situ liquid-phase TEM approach to imaging the nucleation of zeolitic imidazolate framework-8 (ZIF-8) nanocrystals from a solution by using an ultralow electron flux of <0.05 e^{-} $Å^{-2}$ s^{-1}. We chose ZIF-8 MOFs because they are the most prevalently used model structure (the crystal is made up of Zn-coordinated imidazole rings) that can be easily synthesized from an aqueous solution at room temperature (35–38), At ultralow electron fluxes, high spatial resolutions (<1 nm) needed to track the crystallization steps in nucleation events are practically impossible for dynamic TEM imaging. Therefore, to unambiguously observe and validate the crystallization process, we chose to study nucleation of cuboidal MOF nanocrystals (Fig. 1*A*) that are readily obtained by adding 0.5 mM cetyltrimethylammonium bromide (CTAB) surfactant into an aqueous precursor solution for ZIF-8, which contains 13 mM $Zn(NO_3)_2{\cdot}6H_2O$ and 740 mM 2-methylimidazole (39) (*Materials and Methods* and *SI Appendix*, Fig. S1). First, using cryo-TEM imaging, we established that almost all cuboidal MOFs that form from the solution are crystalline (≈99% of MOF nanocubes show clear diffraction spots consistent with ZIF-8 crystal structure) (Fig. 1*B*). Hence, we can use the cuboidal shape of MOFs as an unambiguous indicator of their crystallinity.

The evolution dynamics of ZIF-8 nanocubes from a solution captured by in situ liquid-phase TEM is shown in the post-processed time-resolved image in Fig. 1*C*. The image series reveals three distinct stages through which these MOF nanocrystals form (Movies S1 and S2 are processed and raw [unprocessed] ultralow electron flux movies, respectively). These sequential nucleation steps are 1) phase separation of the reaction solution into solute-rich and solute-poor regions (Fig. 1*C*: t = 15 s) and 2) gradual condensation of the solute-rich regions (i.e., dense liquid phase) (Fig. 1*C*: t = 31 s) into denser aggregates, which then 3) transform into cuboidal nanoparticles (Fig. 1*C*: t = 62 s). As we show in Fig. 1 *A* and *B*, these nanocubes are the MOF crystals. Despite revealing the evolution dynamics of individual cuboidal MOF nanocrystals, these observations still lack the spatial resolution necessary for identifying the phases of the intermediate structures before the nanocubes form. Moreover, it is important to establish that the nucleation pathway observed in situ is generally applicable to MOFs produced under typical synthesis conditions.

To establish the exact characteristics of the intermediate solute-rich phase and validate that the crystallization of MOFs

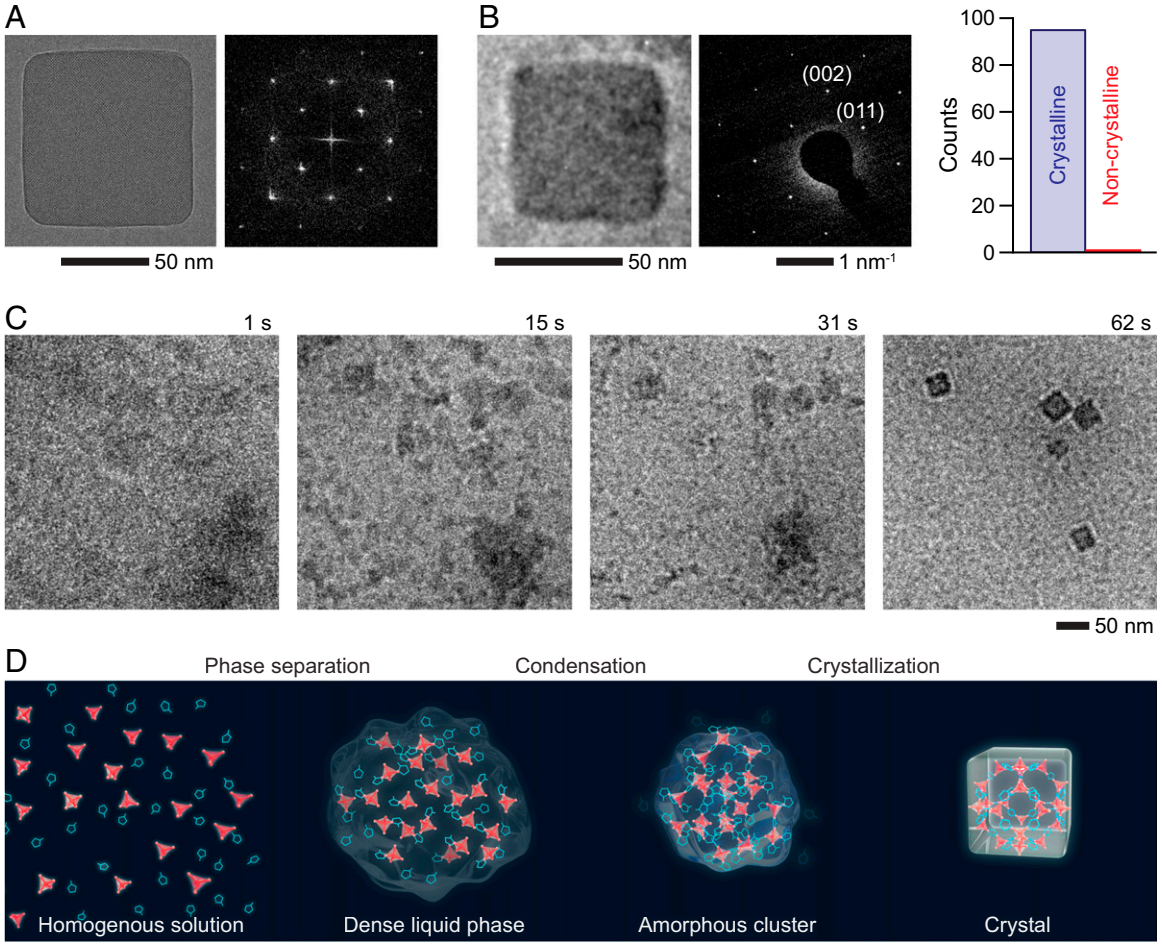

Fig. 1. Nucleation pathway of cuboidal ZIF-8 nanocrystals. (*A*) TEM image (*Left*) and the corresponding Fourier transform (*Right*) of a ZIF-8 nanocube. (*B*) Cryo-TEM image (*Left*) and the corresponding electron diffraction pattern (*Center*) of a typical ZIF-8 nanocube. Out of 95 nanocubes, 94 (≈99%) display clear diffraction patterns consistent with crystalline ZIF-8 (*Right*). (*C*) Time series of in situ TEM images showing the formation of ZIF-8 nanocubes from a reaction solution (see Movies S1 and S2 for processed and raw image series, respectively). Here, the solution (t = 1 s) phase separates into solute-rich (dark gray contrast) and solute-poor (lighter gray contrast) regions (t = 15 s). Next, these solute-rich regions condense into aggregates (t = 31 s), which then crystallize into ZIF-8 nanocubes (t = 62 s) similar to that shown in *B*. (*D*) Schematic illustration of the nucleation process. See *SI Appendix*, Fig. S2 and Movie S3 for additional experimental results taken under the same conditions.

during a bench top synthesis follows the same pathway as the one observed in in situ liquid-phase TEM experiments (Fig. 1 *C* and *D*), we studied the reaction solutions plunge frozen at different reaction time points using cryo-TEM and electron diffraction imaging (Fig. 2). The cryo-TEM images offer a snapshot of the intermediate and final reaction products (Fig. 2*A*), free of any possible electron-beam-induced artifacts, whereas their corresponding diffraction patterns as shown in Fig. 2*B* reveal the crystallinity of the products (25). At $t = 10$ s, the initial reaction solution, for the most part, is homogeneously mixed (Fig. 2*A*). Seldom, we find very small ($\lesssim 5$ nm) clusters (*SI Appendix*, Fig. S3), which are most likely small complexes of Zn^{2+} ions and 2-methylimidazole linkers that may spontaneously form before the obvious phase separation of the reactants in a solution (40). In the cryo-TEM images taken at $t = 60$ s (Fig. 2*A*), we observe an intermediate solute-rich phase consistent with the in situ experiments (Fig. 1*C*: $t = 15$ s). Furthermore, the solution frozen at $t = 120$ s (Fig. 2*A*) displays amorphous aggregates (Fig. 2*B*) that are denser (darker contrast) and smaller in size than the solute-rich liquid phase at $t = 60$ s (Fig. 2*A*). This trend showing the condensation of the solute-rich phase into an amorphous aggregate is again consistent with the in situ condensation process (Fig. 1*C*: $t = 15$ to 31 s). In fact, in our cryo-TEM images acquired at later reaction stages (*SI Appendix*, Fig. S5), we occasionally capture amorphous nanoparticles that just started to resemble nanocubes (similar to our in situ results, Figs. 1*C* and 3*A*: $t = 31$ s) but still lack clear cuboidal morphology, implying that the crystallization has not occurred yet. Finally, the reaction solution frozen at $t = 300$ s (Fig. 2*A*) displays crystalline MOFs with a well-defined cuboidal shape similar to the in situ end products (Fig. 1*C*: $t = 62$ s) and diffraction spots consistent with the crystal structure of ZIF-8 (Fig. 2*B*) (35). To underscore the importance of combining direct time-resolved imaging with cryo-TEM imaging when describing dynamic processes, we highlight here that our conclusions from these results differ from a recent study based on cryo-TEM imaging, which found that amorphous aggregates form first and then dissolve and crystallize into MOFs (41). The crystallization steps from our in situ liquid-phase TEM studies and our cryo-TEM imaging and diffraction studies show that an amorphous aggregate, which serves as a direct precursor for MOF crystallization, forms from the condensation of the solute-rich phase. Thus, the liquid–liquid phase separation is the first critical prenucleation step for MOF formation, which was overlooked by earlier models for MOF nucleation (30, 31, 41).

To better understand how solute-rich phases transform into ZIF-8 nanocubes, we tracked their evolution dynamics in detail (Fig. 3). The solute-rich regions display a viscous fluidlike behavior (Fig. 3 *A–C*) prior to their condensation (into amorphous aggregates) and crystallization as seen from the gradual increase in their TEM image contrasts (21). However, not all of the solute-rich regions transform into aggregates. Fig. 3 *D* and *E* shows how solute-rich phases emerge from the solution only to redissolve and disappear back into the solution without forming any dense aggregates. The likelihood of condensation and dissolution of the metastable solute-rich phase has implications for the nucleation rates and overall synthesis of MOFs because the crystallization is possible only when the solute-rich phase condenses into an amorphous aggregate.

To identify the origin of the interactions that drive the observed phase separation of the solution into solute-rich and solute-poor regions (Fig. 1*C*), we performed molecular dynamics (MD) simulations. In these simulations, we tracked the trajectory of interacting complexes that form when 2-methylimidazole linkers react with Zn^{2+} ions (*SI Appendix*, *Molecular Dynamics Simulations*). These complexes can come in many different sizes, but for simplicity, we only considered complexes of three different sizes (*SI Appendix*, Fig. S8), which are sufficient to qualitatively describe how the liquid–liquid phase separation occurs. Furthermore, CTAB that stabilizes the side facets of a cuboidal MOF in our experiments was also omitted from these simulations because the simulations focus only on the phase separation of reactants and their subsequent aggregation. We tested three types of complexes. The first type is nonpolar complexes with zero net charge, which did not phase separate to form aggregates and remained dispersed within the solution (*SI Appendix*, Figs. S8 *A–C* and S9). Charged complexes, which are the second type, assemble into very rigid amorphous structures that will not transition into crystalline MOFs (*SI Appendix*, Fig. S11). As a final third case, we tested the interaction of neutral, but polar, complexes (Fig. 4*A*). These polar complexes were neutralized by removing the

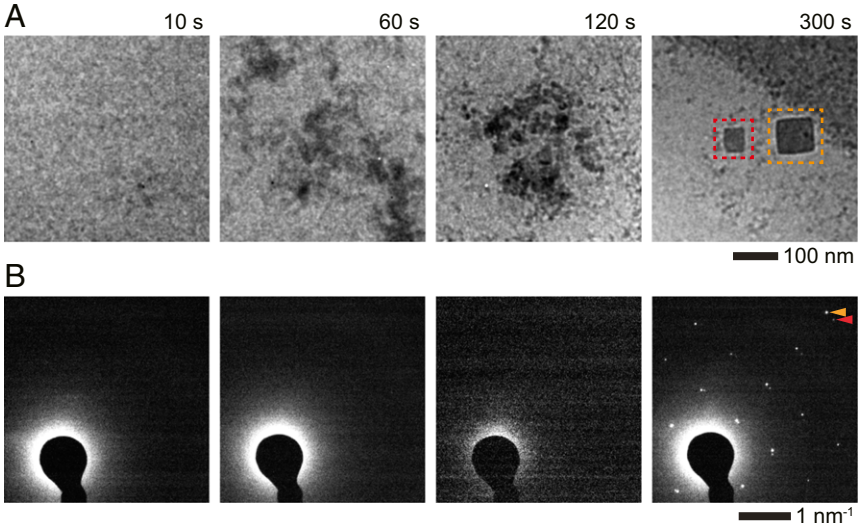

Fig. 2. Cryo-TEM and electron diffraction images showing different stages of MOF nucleation. (*A*) Cryo-TEM images of the room-temperature reaction solutions plunge frozen after 10, 60, 120, and 300 s. These reaction stages compare well with the different stages identified from the in situ observations shown in Fig. 1*C*. (*B*) Selected area diffraction patterns corresponding to the cryo-TEM images in *A* show that only final nanocubes possess the crystalline phase associated with ZIF-8 structure, while all the reaction products prior to this step are amorphous. Also, see *SI Appendix*, Fig. S4 for more cryo-TEM images. The red and orange arrows highlight the (044) diffraction spots from the two different nanocubes in *A* at $t = 300$ s.

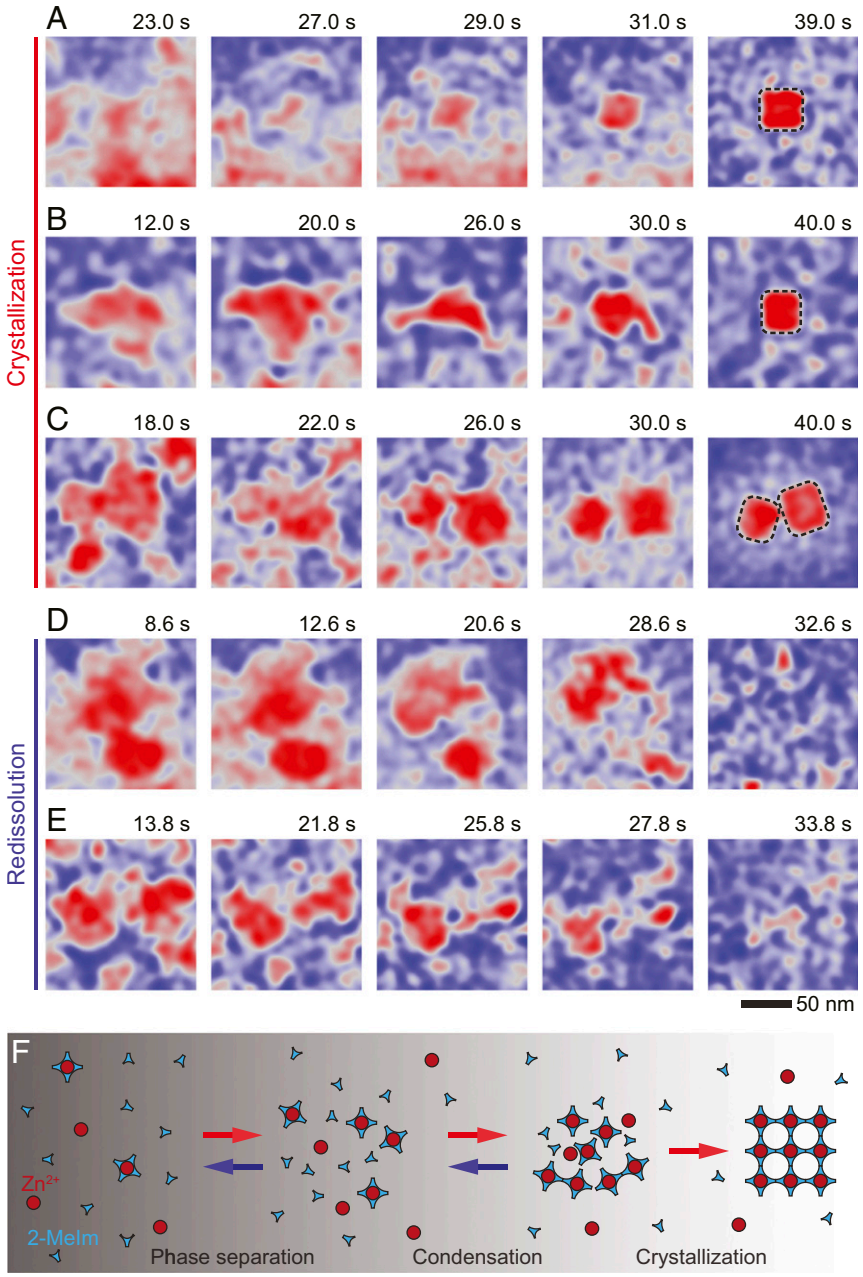

Fig. 3. Evolution dynamics of the fluidlike solute-rich phases. (*A*–*C*) Time series of in situ TEM images showing the gradual condensation of the solute-rich liquid regions into dense aggregates (fourth panel) and then into ZIF-8 nanocubes (Movies S4–S6). The aggregates are direct precursors for cuboidal ZIF-8 nanocrystals. (*D* and *E*) Time series of in situ TEM images showing the dissolution of the solute-rich regions back into the solution (Movies S7 and S8). In both cases, solute-rich regions are highly dynamic and display fluidlike behavior. (*F*) Schematic illustration showing the crystallization of MOFs from a solution. Red and blue shapes represent Zn^{2+} ions and 2-methylimidazole (2-MeIm), respectively.

appropriate number of protons from 2-methylimidazole (Fig. 4*A*). The simulations tracking the trajectory of these complexes reveal that attractive dipolar interactions between the complexes drive their gradual condensation into gel-like aggregates (Fig. 4*B* and *SI Appendix*, Fig. S12), and the strength of the dipolar interactions increases with the size of the complexes (*SI Appendix*, Fig. S13). The condensation of the solute-rich phase into amorphous aggregates is best described by plotting the time-dependent evolution of the cluster size distribution represented in the form of the Zn atoms within the cluster. This plot in Fig. 4*C* reveals the emergence of larger aggregates as the number of smaller complexes decreases. While MD simulations cannot describe the crystallization of the aggregates, the flexible nature of the aggregates hints that the nucleation most likely occurs by a sequential recrystallization process involving the formation and breaking of the relevant bonds within the aggregates as redundant molecules are expelled (42, 43).

To comment on the observed redissolution of the metastable solute-rich phase (Fig. 3 *D* and *E*), we speculate that the redissolution may occur due to the low concentration of metal ions (Zn^{2+}). To test this hypothesis, we imaged the solutions containing only 2-methylimidazole using cryo-TEM (*SI Appendix*, Fig. S6), and consistent with our hypothesis, we did not find any crystalline MOFs or traces of dense liquid phase (i.e., solid-rich regions) and amorphous aggregates, indicating that the solution did not phase separate at low solute concentrations. These observations are consistent with our MD simulations, which predict

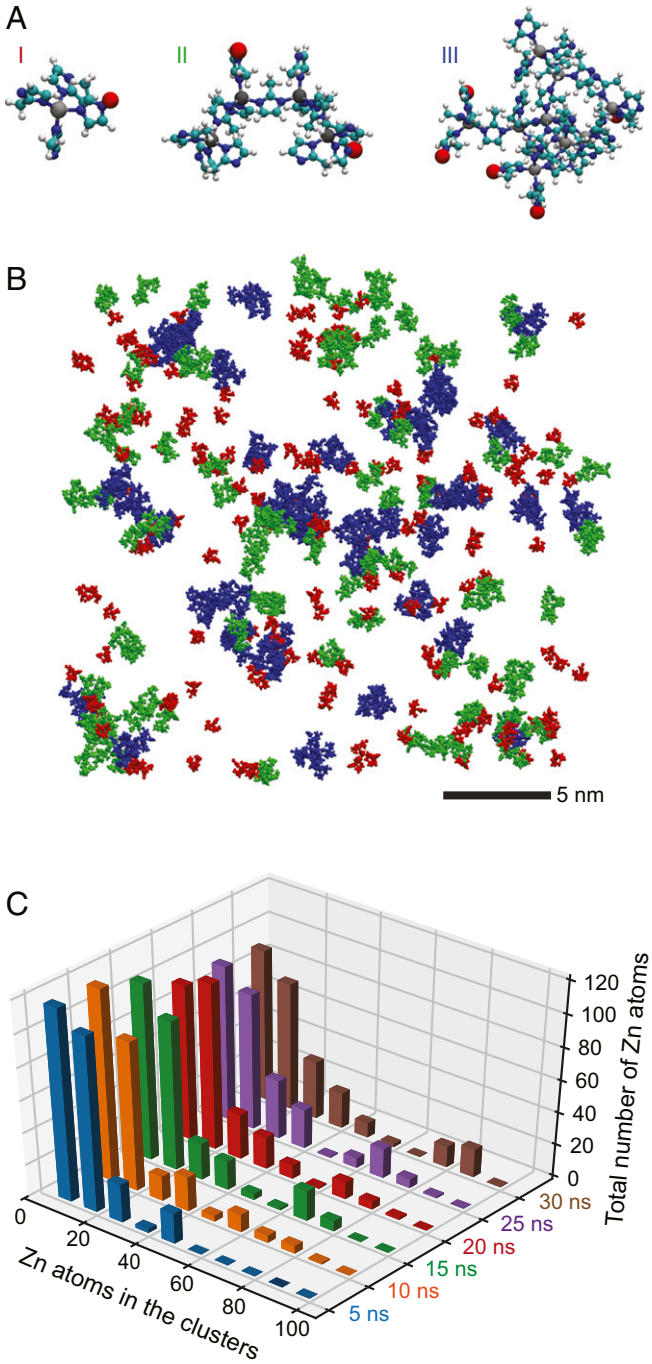

Fig. 4. MD simulations of aggregation of initial MOF building blocks. (*A*) The structures of polar molecular complexes comprising 2-methylimidazole and 2, 6, and 14 Zn atoms were used for the MD simulation. Gray, blue, green, and white spheres represent Zn, N, C, and H atoms, respectively. Red spheres represent the Zn atoms that replace protons of the 2-methylimidazole unit. (*B*) Snapshot of the system comprising complexes shown in *A* undergoing assembly in 30 ns (see *SI Appendix*, Fig. S13 for entire time evolution). Red, green, and blue complexes correspond to molecules I, II, and III in *A*. (*C*) A total count of the clusters composed of different numbers of Zn atoms at different simulation times.

that linkers with low Zn^{2+} content interact weakly and do not readily phase separate into solute-rich regions within the simulation timescales (*SI Appendix*, *Molecular Dynamics Simulations*).

Comparing the observed crystallization to the existing nucleation models for MOFs and other classes of materials with topologically similar structures can highlight how the difference in intermediate structures might affect the overall crystallization process. For example, in the case of zeolites, microporous aluminosilicates, whose nucleation and growth have been explored in great detail because of their importance for catalysis (44), nucleation occurs through a two-step process (45). These steps are the formation of intermediate stable gel-like precursors via monomer aggregation and crystallization of zeolites deep within these gels (46, 47). The current models for MOF crystallization bear a resemblance somewhat similar to the crystallization pathway of zeolites and propose that linkers and metal ion complexes form small solid clusters via coagulation, which then grow into amorphous nanoparticles by monomer addition, followed by crystallization of these stable nanoparticles (30, 31). Again, these indirect models contrast our direct observations, which identify phase separation and condensation of the metastable fluidlike solute-rich phase to be the key steps that produce local regions with high reactant concentrations needed for crystals to form.

Although our observations show a metastable amorphous aggregate to be a direct precursor for MOF crystallization, they still lack the spatial resolution needed to identify the details of molecular mechanisms involved in the nucleation process. The next big challenge is to determine how individual ions and linkers react in a solute-rich liquid phase and also rearrange within the amorphous aggregates to form MOF crystals. At present, it is not entirely clear whether the crystallization occurs directly during the reaction of monomers or via self-assembly of individual nucleation (40, 48) or a secondary building unit (49, 50) comprising reacted metal ion and linker complexes (51, 52) and when and how these building units form. Moreover, we note that MOFs are also often synthesized through different solvents and at elevated temperatures, all of which affect the reaction outcome (38, 53). At present, imaging beam-sensitive materials is challenging because, at elevated temperatures, the electron beam can significantly alter reaction chemistry (54, 55). We envision that with the further improvement in liquid cell reactors, detectors, and imaging methods and analysis, we will be able to explore the crystallization processes in such systems with great detail.

Finally, we comment on why ultralow electron flux needs to be maintained during the imaging. First, we had established that the observed formation of the ZIF-8 nanocubes in the liquid cell is not caused by the electron beam by flowing the precursor solution into the cell while keeping the electron beam blanked. After roughly 10 min, we unblanked the beam ($\approx$0.05 e^- $Å^{-2}$ s^{-1}) and acquired the TEM images and found ZIF-8 nanocubes in the field of view. These nanocubes start to dissolve only after approximately 100 s of imaging, indicating the onset of beam-induced effects at a very low cumulative dose of 5 e^- $Å^{-2}$ (*SI Appendix*, Fig. S7).

Conclusions

Our observations clearly show that, in an aqueous solution, zeolitic imidazolate framework nanocrystals nucleate through a sequence of three distinct steps that are not accounted for by current nucleation models for MOFs and other porous crystalline structures. These stages are phase separation of the reaction solution into solute-rich and solute-poor phases, followed by direct condensation of the metastable solute-rich phases into amorphous aggregates, which then crystallize to form MOF nanoparticles. We expect the observed sequence of nucleation steps to be general for the crystallization process and amorphous aggregates to be a prenucleation precursor directly responsible for the formation of a crystalline phase. The broader significance of our approach is that it enables direct imaging of elusive pathways through which many beam-sensitive materials may form and transform. Extending these kinds of studies to biological and other organic molecules will be essential for developing a better and broadly applicable framework that can describe how different classes of materials form from a solution.

Materials and Methods

Chemical Reagents. The reagents used in this study are zinc nitrate hexahydrate [$Zn(NO_3)_2{\cdot}6H_2O$; catalog number 520918-5G, Sigma-Aldrich Co.], 2-methylimidazole (catalog number M50850-100G, Sigma-Aldrich Co.), and CTAB (catalog number 52370-500G, Sigma-Aldrich Co.). These reagents were used as received without further purification. Solutions were prepared using deionized water with a resistivity of 18.2 MΩ cm.

Synthesis of Cuboidal ZIF-8 Nanoparticles. To synthesize the ZIF-8 nanocubes, we followed the protocol developed by Chou et al. (39), where we optimized the reactant concentrations and reaction times of their protocol to make it more suitable for our in situ studies. For a typical synthesis, the reaction solution for synthesizing ZIF-8 nanocubes was prepared by mixing 0.1 mL of 195 mM $Zn(NO_3)_2$, 0.7 mL of 1.58 M 2-methylimidazole, and 0.7 mL of 1.1 mM CTAB solutions at room temperature for up to 10 to 180 min. The final concentrations of $Zn(NO_3)_2$, 2-methylimidazole, and CTAB in the solution were 13 mM, 0.74 M, and 0.51 mM, respectively. Our protocol enabled us to drastically reduce the reaction times needed to obtain the nanocubes. Extending the reaction time causes the nanocubes to grow further (i.e., the size of the nanocubes increases). For example, the nanocubes from 10 and 180 min reactions have side lengths in the range of 30 to 80 and 30 to 100 nm, respectively (*SI Appendix*, Fig. S1 *A* and *B*).

The crystallinity of the samples was confirmed by measuring their X-ray diffraction (XRD) spectra (*SI Appendix*, Fig. S1*C*). Here, the reaction products were washed with deionized water twice by centrifugation at 10,000 rpm for 5 min and resuspension, after which they were dried at 60 °C for 180 min. The XRD measurements were done using a Bruker D8 Advance X-ray diffractometer with a generator power voltage and current of 40 kV and 40 mA, respectively (Bruker Singapore Pte. Ltd.).

In Situ TEM Imaging Experiments. Each liquid cell was assembled from two custom microfabricated 2.6×2.6 mm^2 Si chips. A chip had a 25-nm-thick SiN_x window with dimensions of 200×25 μm^2 in the center (56). Before in situ experiments, the chips were washed and dried with acetone (catalog number 650501-1L, Sigma-Aldrich Co.), isopropyl alcohol (catalog number 650501-1L, Sigma-Aldrich Co.), and deionized water. Before assembling in the TEM flow holder (Hummingbird Scientific), the chips were treated with oxygen plasma using an Emitech K100X glow discharge unit (Quorum Technologies) to render their surfaces hydrophilic. The treatment was done by setting the plasma current to 15 mA with negative discharge polarity for a duration of 45 s. Next, the liquid cells were assembled inside the TEM flow holder while ensuring that the membranes from the bottom and top chips were aligned, and then the holder was inserted in a TEM for in situ imaging. After quickly checking that the TEM was aligned and the membrane windows were visible under the electron beam, we prepared a fresh precursor solution for MOF synthesis, loaded it into a syringe, and flowed it into the liquid cell at a flow rate of 5 μL min^{-1} until the solution reached the window area of the liquid cell. It takes about 1 to 2 min for the freshly prepared precursor solution to reach the SiN_x membrane windows. Once the solution reaches the membrane windows, we imaged the solution with an electron beam at a flux of $\leq$0.05 e^- $Å^{-2}$ s^{-1}. The typical thickness of the solution sandwiched between the two SiN_x membrane windows in these liquid cells ranges from 100 to 300 nm (57). To underscore the importance of rapid loading of fresh precursor solution in capturing the crystallization events, we mention that when there is a significant delay between the loading of precursor solution into the cells and imaging, we would occasionally miss the crystallization process and find MOF nanocubes to be already present in the solution upon imaging.

Cryo-TEM Imaging Experiments. To prepare samples for cryo-TEM imaging, we applied 3.5 μL of the reaction solution onto freshly plasma cleaned Quantifoil TEM grids (200 mesh Cu TEM grid Quantifoil holey carbon films with 2 μm holes, R 2/2; Quantifoil Micro Tools GmbH). The reaction solutions were applied to the TEM grids immediately after the solutions were prepared and then plunge frozen in cooled liquid ethane using the automated vitrification robot (FEI Vitrobot Mark IV; Thermo Fisher Scientific Ltd.) after 10, 60, 120, 180, and 300 s of their preparation. Note that for each reaction time, we prepared at least three different solutions and imaged multiple areas of the grids. For example, as mentioned in Fig. 1*C*, 95 nanocubes were imaged to unequivocally establish the relationship between the cuboidal shape and the crystallinity of ZIF-8 nanocubes.

TEM Imaging and Image Processing. All TEM images and movies were acquired using a JEOL 2200FS TEM with an accelerating voltage of 200 kV (JEOL Ltd.). Cryo-TEM images and images from drop casted and dried specimens were recorded using an Orius SC200 CCD TEM camera (Gatan, Inc.). The in situ liquid phase TEM movies were recorded at a frame rate of 20 frames per second and at a magnification ranging from 8,000× to 20,000× using a DE-16 direct detector (Direct Electron, LP). For the in situ imaging, we maintained the electron flux at $\leq$0.05 e^- $Å^{-2}$ s^{-1}. High-resolution TEM images, similar to those shown in Fig. 1*A*, were taken with an FEI Titan TEM (Thermo Fisher Scientific Ltd.) operated at 300 kV, and the images were recorded with a K2 IS camera (Gatan, Inc.).

To prevent beam-induced artifacts during the in situ TEM imaging of MOF nucleation, we had to use an ultralow electron flux of $\leq$0.05 e^- $Å^{-2}$ s^{-1}. Because of this low-flux imaging condition, the raw in situ TEM image series were extremely noisy and very difficult to interpret (Movie S2). To improve the image contrast, first, we averaged five consecutive raw frames in an image sequence file and performed drift correction across the averaged frames using the template matching and slice alignment plugin (58, 59) in ImageJ (60). Second, the drift correction parameters obtained from ImageJ were further smoothened by fitting them to a sixth-degree polynomial using the NumPy (61) and OpenCV (62) library in Python version 2.7 (63). Third, we applied the drift correction parameters from the polynomial fit to all the raw frames. Fourth, we then reaveraged five consecutive drift-corrected frames to improve the signal-to-noise ratio of the images. Fifth, we applied a three-dimensional Gaussian filter with $\sigma_x = \sigma_y = 0$ pixels and $\sigma_z = 5$ pixels to remove high-frequency features. Here, z is the time axis of the image stack. This processing produced images with a much better contrast (Movie S1). Also, note that the images in Fig. 3 were false colored using the "UnionJack" color scheme in ImageJ; the processed movies corresponding to Fig. 3 are provided as Movies S4–S8.

Molecular Dynamics Simulations. MD simulations were performed with the NAMD (Nanoscale Molecular Dynamics) software package (64) in an *NPT* ensemble at $T = 300$ K, using the Langevin dynamics with a damping constant of $\gamma_{\text{Lang}} = 0.1$ ps^{-1} and a time step of 2 fs. The CHARMM (Chemistry at Harvard Macromolecular Mechanics) general force field (65, 66) was implemented for the bond, angle, and dihedral parameters of the water molecules and different complexes comprising linkers and Zn ions. Nonbonding interactions between these molecules, such as a van der Waals (vdW) attraction and a steric repulsion, were described by the Lennard-Jones (LJ) potential,

$$U_{LJ}(r) = \varepsilon\left[\left(\frac{r_{\min}}{r}\right)^{12} - 2\left(\frac{r_{\min}}{r}\right)^{6}\right],$$

where ε is the minimum (negative) energy of the coupling and $r_{\min}$ is a distance where $U_{LJ}(r_{\min})$ has a local minimum, both of which are provided by the CHARMM force field. Here, the r^{-12} and r^{-6} terms represent an atomic repulsion due to overlapping electron orbitals and the vdW attractive coupling, respectively. The LJ potential implemented in NAMD has a typical cutoff distance of 1 nm. The electrostatic coupling between ions and partially charged atoms, which also belongs to nonbonding interactions, has a cutoff similar to that of the LJ potential, but its long-range part is calculated by the particle mesh Ewald (PME) method (67) in the presence of periodic boundary conditions.

To obtain the initial force field parameters of the simulated molecules, we prepared all the structures by replacing Zn atoms with tetrahedral C atoms. Once the different types of complexes were tested in our simulations and their corresponding charges were obtained from the CHARMM force field, we used the VMD force field toolkit plugin to find appropriate parameters for all the structures after subsequent replacement of C and Zn atoms.

Data Availability. All study data are included in the article and/or *SI Appendix*.

ACKNOWLEDGMENTS. This work was supported by the Singapore National Research Foundation's Competitive Research Program funding (grant number: NRF-CRP16-2015-05).

1. J. Lee *et al.*, Metal-organic framework materials as catalysts. *Chem. Soc. Rev.* **38**, 1450–1459 (2009).
2. N. L. Rosi *et al.*, Hydrogen storage in microporous metal-organic frameworks. *Science* **300**, 1127–1129 (2003).
3. H. Li, M. Eddaoudi, T. L. Groy, O. M. Yaghi, Establishing microporosity in open metal–organic frameworks: Gas sorption isotherms for Zn(BDC) (BDC = 1,4-benzenedicarboxylate). *J. Am. Chem. Soc.* **120**, 8571–8572 (1998).
4. H. Furukawa, K. E. Cordova, M. O'Keeffe, O. M. Yaghi, The chemistry and applications of metal-organic frameworks. *Science* **341**, 1230444 (2013).
5. O. M. Yaghi *et al.*, Reticular synthesis and the design of new materials. *Nature* **423**, 705–714 (2003).
6. S. Saha, M. Wiebcke, K. Huber, Insight into fast nucleation and growth of zeolitic imidazolate framework-71 by in situ static light scattering at variable temperature and kinetic modeling. *Cryst. Growth Des.* **18**, 4653–4661 (2018).

7. M. Eddaoudi *et al*., Systematic design of pore size and functionality in isoreticular MOFs and their application in methane storage. *Science* **295**, 469–472 (2002).
8. M. J. Van Vleet, T. Weng, X. Li, J. R. Schmidt, In situ, time-resolved, and mechanistic studies of metal-organic framework nucleation and growth. *Chem. Rev.* **118**, 3681–3721 (2018).
9. J. D. Rimer, M. Tsapatsis, Nucleation of open framework materials: Navigating the voids. *MRS Bull.* **41**, 393–398 (2016).
10. J. De Yoreo, Crystal nucleation: More than one pathway. *Nat. Mater.* **12**, 284–285 (2013).
11. P. G. Vekilov, Nucleation. *Cryst. Growth Des.* **10**, 5007–5019 (2010).
12. P. G. Vekilov, Dense liquid precursor for the nucleation of ordered solid phases from solution. *Cryst. Growth Des.* **4**, 671–685 (2004).
13. J. J. De Yoreo, P. G. Vekilov, Principles of crystal nucleation and growth. *Rev. Mineral. Geochem.* **54**, 57–93 (2003).
14. V. I. Kalikmanov, "Classical nucleation theory" in *Nucleation Theory* (Springer, 2013), pp. 17–41.
15. P. G. Vekilov, The two-step mechanism of nucleation of crystals in solution. *Nanoscale* **2**, 2346–2357 (2010).
16. J. J. De Yoreo *et al*., Crystallization by particle attachment in synthetic, biogenic, and geologic environments. *Science* **349**, aaa6760 (2015).
17. Y. Tsarfati *et al*., Crystallization of organic molecules: Nonclassical mechanism revealed by direct imaging. *ACS Cent. Sci.* **4**, 1031–1036 (2018).
18. P. J. M. Smeets *et al*., A classical view on nonclassical nucleation. *Proc. Natl. Acad. Sci. U.S.A.* **114**, E7882–E7890 (2017).
19. R. J. Davey, S. L. M. Schroeder, J. H. ter Horst, Nucleation of organic crystals—A molecular perspective. *Angew. Chem. Int. Ed. Engl.* **52**, 2166–2179 (2013).
20. R. J. Davey, K. R. Back, R. A. Sullivan, Crystal nucleation from solutions—Transition states, rate determining steps and complexity. *Faraday Discuss.* **179**, 9–26 (2015).
21. N. D. Loh *et al*., Multistep nucleation of nanocrystals in aqueous solution. *Nat. Chem.* **9**, 77–82 (2017).
22. J. Zhou *et al*., Observing crystal nucleation in four dimensions using atomic electron tomography. *Nature* **570**, 500–503 (2019).
23. O. Galkin, P. G. Vekilov, Are nucleation kinetics of protein crystals similar to those of liquid droplets? *J. Am. Chem. Soc.* **122**, 156–163 (2000).
24. D. Gebauer, A. Völkel, H. Cölfen, Stable prenucleation calcium carbonate clusters. *Science* **322**, 1819–1822 (2008).
25. E. M. Pouget *et al*., The initial stages of template-controlled $CaCO_3$ formation revealed by cryo-TEM. *Science* **323**, 1455–1458 (2009).
26. M. H. Nielsen, S. Aloni, J. J. De Yoreo, In situ TEM imaging of $CaCO_3$ nucleation reveals coexistence of direct and indirect pathways. *Science* **345**, 1158–1162 (2014).
27. H. Du, E. Amstad, Water: How does it influence the $CaCO_3$ formation? *Angew. Chem. Int. Ed. Engl.* **59**, 1798–1816 (2020).
28. F. Millange *et al*., Time-resolved in situ diffraction study of the solvothermal crystallization of some prototypical metal-organic frameworks. *Angew. Chem. Int. Ed. Engl.* **49**, 763–766 (2010).
29. X. G. Wang, Q. Cheng, Y. Yu, X. Z. Zhang, Controlled nucleation and controlled growth for size predicable synthesis of nanoscale metal-organic frameworks (MOFs): A general and scalable approach. *Angew. Chem. Int. Ed. Engl.* **57**, 7836–7840 (2018).
30. J. Cravillon *et al*., Fast nucleation and growth of ZIF-8 nanocrystals monitored by time-resolved in situ small-angle and wide-angle X-ray scattering. *Angew. Chem. Int. Ed. Engl.* **50**, 8067–8071 (2011).
31. S. Saha *et al*., Insight into fast nucleation and growth of zeolitic imidazolate framework-71 by in situ time-resolved light and X-ray scattering experiments. *Cryst. Growth Des.* **16**, 2002–2010 (2016).
32. H. Xu, S. Sommer, N. L. N. Broge, J. Gao, B. B. Iversen, The chemistry of nucleation: In situ pair distribution function analysis of secondary building units during UiO-66 MOF formation. *Chemistry* **25**, 2051–2058 (2019).
33. J. P. Patterson *et al*., Observing the growth of metal-organic frameworks by in situ liquid cell transmission electron microscopy. *J. Am. Chem. Soc.* **137**, 7322–7328 (2015).
34. Y. Zhu *et al*., Unravelling surface and interfacial structures of a metal-organic framework by transmission electron microscopy. *Nat. Mater.* **16**, 532–536 (2017).
35. K. S. Park *et al*., Exceptional chemical and thermal stability of zeolitic imidazolate frameworks. *Proc. Natl. Acad. Sci. U.S.A.* **103**, 10186–10191 (2006).
36. X. C. Huang, Y. Y. Lin, J. P. Zhang, X. M. Chen, Ligand-directed strategy for zeolite-type metal-organic frameworks: Zinc(II) imidazolates with unusual zeolitic topologies. *Angew. Chem. Int. Ed. Engl.* **45**, 1557–1559 (2006).
37. Y. Pan *et al*., Tuning the crystal morphology and size of zeolitic imidazolate framework-8 in aqueous solution by surfactants. *CrystEngComm* **13**, 6937–6940 (2011).
38. N. Stock, S. Biswas, Synthesis of metal-organic frameworks (MOFs): Routes to various MOF topologies, morphologies, and composites. *Chem. Rev.* **112**, 933–969 (2012).
39. L. Y. Chou *et al*., Formation of hollow and mesoporous structures in single-crystalline microcrystals of metal-organic frameworks via double-solvent mediated overgrowth. *Nanoscale* **7**, 19408–19412 (2015).
40. M. W. Terban *et al*., Early stage structural development of prototypical zeolitic imidazolate framework (ZIF) in solution. *Nanoscale* **10**, 4291–4300 (2018).
41. A. F. Ogata *et al*., Direct observation of amorphous precursor phases in the nucleation of protein-metal-organic frameworks. *J. Am. Chem. Soc.* **142**, 1433–1442 (2020).
42. M. C. Bernini *et al*., Reversible breaking and forming of metal-ligand coordination bonds: Temperature-triggered single-crystal to single-crystal transformation in a metal-organic framework. *Chemistry* **15**, 4896–4905 (2009).
43. R. S. K. Madsen *et al*., Ultrahigh-field ^{67}Zn NMR reveals short-range disorder in zeolitic imidazolate framework glasses. *Science* **367**, 1473–1476 (2020).
44. J. Weitkamp, Zeolites and catalysis. *Solid State Ion.* **131**, 175–188 (2000).
45. J. Grand, H. Awala, S. Mintova, Mechanism of zeolites crystal growth: New findings and open questions. *CrystEngComm* **18**, 650–664 (2016).
46. S. Mintova, N. H. Olson, V. Valtchev, T. Bein, Mechanism of zeolite A nanocrystal growth from colloids at room temperature. *Science* **283**, 958–960 (1999).
47. S. Mintova, N. H. Olson, T. Bein, Electron microscopy reveals the nucleation mechanism of zeolite Y from precursor colloids. *Angew. Chem. Int. Ed. Engl.* **38**, 3201–3204 (1999).
48. G. Férey, Building units design and scale chemistry. *J. Solid State Chem.* **152**, 37–48 (2000).
49. M. Eddaoudi *et al*., Modular chemistry: Secondary building units as a basis for the design of highly porous and robust metal-organic carboxylate frameworks. *Acc. Chem. Res.* **34**, 319–330 (2001).
50. G. Férey, M. Haouas, T. Loiseau, F. Taulelle, Nanoporous solids: How do they form? An in situ approach. *Chem. Mater.* **26**, 299–309 (2013).
51. D. C. Cantu, B. P. McGrail, V.-A. Glezakou, Formation mechanism of the secondary building unit in a chromium terephthalate metal–organic framework. *Chem. Mater.* **26**, 6401–6409 (2014).
52. L. Kollias *et al*., Molecular level understanding of the free energy landscape in early stages of metal-organic framework nucleation. *J. Am. Chem. Soc.* **141**, 6073–6081 (2019).
53. M. Lanchas *et al*., A direct reaction approach for the synthesis of zeolitic imidazolate frameworks: Template and temperature mediated control on network topology and crystal size. *Chem. Commun. (Camb.)* **48**, 9930–9932 (2012).
54. J. T. van Omme *et al*., Liquid phase transmission electron microscopy with flow and temperature control. *J. Mater. Chem. C* **8**, 10781–10790 (2020).
55. S. W. Chee, S. F. Tan, Z. Baraissov, M. Bosman, U. Mirsaidov, Direct observation of the nanoscale Kirkendall effect during galvanic replacement reactions. *Nat. Commun.* **8**, 1224 (2017).
56. G. Lin, S. W. Chee, S. Raj, P. Král, U. Mirsaidov, Linker-mediated self-assembly dynamics of charged nanoparticles. *ACS Nano* **10**, 7443–7450 (2016).
57. S. W. Chee, Z. Baraissov, N. D. Loh, P. T. Matsudaira, U. Mirsaidov, Desorption-mediated motion of nanoparticles at the liquid–solid interface. *J. Phys. Chem. C* **120**, 20462–20470 (2016).
58. Q. Tseng *et al*., A new micropatterning method of soft substrates reveals that different tumorigenic signals can promote or reduce cell contraction levels. *Lab Chip* **11**, 2231–2240 (2011).
59. Q. Tseng *et al*., Spatial organization of the extracellular matrix regulates cell-cell junction positioning. *Proc. Natl. Acad. Sci. U.S.A.* **109**, 1506–1511 (2012).
60. C. A. Schneider, W. S. Rasband, K. W. Eliceiri, NIH image to ImageJ: 25 years of image analysis. *Nat. Methods* **9**, 671–675 (2012).
61. S. d. Walt, S. C. Colbert, G. Varoquaux, The NumPy array: A structure for efficient numerical computation. *Comput. Sci. Eng.* **13**, 22–30 (2011).
62. G. Bradski, A. Kaehler, *Learning OpenCV: Computer Vision with the OpenCV Library* (O'Reilly Media, 2008).
63. T. E. Oliphant, Python for scientific computing. *Comput. Sci. Eng.* **9**, 10–20 (2007).
64. J. C. Phillips *et al*., Scalable molecular dynamics with NAMD. *J. Comput. Chem.* **26**, 1781–1802 (2005).
65. K. Vanommeslaeghe *et al*., CHARMM General Force Field: A force field for drug-like molecules compatible with the CHARMM all-atom additive biological force fields. *J. Comput. Chem.* **31**, 671–690 (2010).
66. W. Yu, X. He, K. Vanommeslaeghe, A. D. MacKerell Jr, Extension of the CHARMM General Force Field to sulfonyl-containing compounds and its utility in biomolecular simulations. *J. Comput. Chem.* **33**, 2451–2468 (2012).
67. T. Darden, D. York, L. Pedersen, Particle mesh Ewald: An N·log(N) method for Ewald sums in large systems. *J. Chem. Phys.* **98**, 10089–10092 (1993).